Geochemistry Geophysics Geosystems G3
AN ELECTRONIC JOURNAL OF THE EARTH SCIENCES
Published by AGU and the Geochemical Society

Article
Volume 6, Number 11
4 November 2005
Q11002, doi:10.1029/2005GC000943
ISSN: 1525-2027

Variations in upper crustal structure due to variable mantle temperature along the Southeast Indian Ridge

Janet M. Baran, James R. Cochran, Suzanne M. Carbotte, and Mladen R. Nedimović
Lamont-Doherty Earth Observatory of Columbia University, 61 Route 9W, Palisades, New York 10964, USA (baran@ldeo.columbia.edu)

[1] There is a systematic variation in axial morphology and axial depth along the Southeast Indian Ridge (SEIR) with distance away from the Australian Antarctic Discordance, an area of cold uppermost mantle. Since spreading rate (72–76 mm/yr) and mantle geochemistry appear constant along this portion of the SEIR, the observed variations in axial morphology and axial depth are attributed to a gradient in mantle temperature. In this study, we report results from a multichannel seismic investigation of on-axis crustal structure along this portion of the SEIR. Three distinct forms of ridge crest morphology are found within our study area: axial highs, rifted axial highs, and shallow axial valleys. Axial highs have a shallow (~1500 m below seafloor (bsf)) magma lens and a thin (~300 m) layer 2A along the ridge crest. Rifted axial highs have a deeper (~2100 m bsf) magma lens and thicker (~450 m) layer 2A on-axis. Beneath shallow axial valleys, no magma lens is imaged, and layer 2A is thick (~450 + m). There are step-like transitions in magma lens depth and layer 2A thickness with changes in morphology along the SEIR. The transitions between the different modes of axial morphology and shallow structure are abrupt, suggesting a threshold-type mechanism. Variations in crustal structure along the SEIR appear to be steady state, persisting for at least 1 m.y. Portions of segments in which a magma lens is found are characterized by lower relief abyssal hills on the ridge flank, shallower ridge flank depths, and at the location of along-axis Mantle Bouguer Anomaly (MBA) lows. The long-wavelength variation in ridge morphology along the SEIR from axial high segments to the west to axial valley segments to the east is linked to the regional gradient in mantle temperature. Superimposed on the long-wavelength trend are segment to segment variations that are related to the absolute motion of the SEIR to the northeast which influence mantle melt production and delivery to the ridge.

Components: 10,963 words, 9 figures.

Keywords: Layer 2A; magma chambers; mid-ocean ridge processes; Southeast Indian Ridge.

Index Terms: 3025 Marine Geology and Geophysics: Marine seismics (0935, 7294); 3035 Marine Geology and Geophysics: Midocean ridge processes; 3045 Marine Geology and Geophysics: Seafloor morphology, geology, and geophysics.

Received 18 February 2005; **Revised** 21 July 2005; **Accepted** 2 September 2005; **Published** 4 November 2005.

Baran, J. M., J. R. Cochran, S. M. Carbotte, and M. R. Nedimović (2005), Variations in upper crustal structure due to variable mantle temperature along the Southeast Indian Ridge, *Geochem. Geophys. Geosyst.*, *6*, Q11002, doi:10.1029/2005GC000943.

1. Introduction

[2] The worldwide system of mid-ocean ridges shows a systematic pattern of morphological and structural characteristics that has been related to spreading rate. Fast spreading ridges are characterized by axial highs, low-relief abyssal hills, magma lenses at shallow depths in the crust, and thin layer 2A at the ridge-axis that thickens off-axis [e.g., *Menard*, 1960; *MacDonald*, 1989; *Detrick et al.*, 1987, 1993; *Christeson et al.*, 1996; *Hooft et al.*, 1996]. Slow spreading ridges are characterized

by axial valleys, large abyssal hills, and thick on-axis layer 2A that does not thicken off-axis [e.g., *Heezen*, 1960; *MacDonald*, 1986; *Hussenoeder et al.*, 2002]. No magma lens has been conclusively imaged to date at a ridge with a well-developed axial valley [*Detrick et al.*, 1990; *Calvert*, 1995, 1997] although a zone of low seismic velocities presumably associated with melt within the crust has been detected deeper in the crust than at fast spreading ridges [*Canales et al.*, 2000].

[3] *Phipps Morgan and Chen* [1993] presented a model for crustal accretion in which the thermal structure at the ridge axis is governed by the balance between heat input to the crust through magma injection and heat removal through hydrothermal circulation. This model predicts that the magma lens will become deeper with decreasing spreading rate. *Purdy et al.* [1992] have presented observations that suggest a systematic relationship between spreading rate, and magma lens depth supporting a *Phipps Morgan and Chen* [1993] type model. At a given spreading rate, the *Phipps Morgan and Chen* [1993] model is very sensitive to magma supply to the crust (crustal thickness) because of the critical role that the latent heat of crystallization plays in maintaining the magma lens.

[4] The morphology and crustal structure observed at fast spreading and at slow-spreading ridge axes represent two very different and distinct modes of ridge axis structure. It is of importance in understanding ridge axis processes to determine how and under what circumstances one mode passes into the other. Acquiring this knowledge requires examination of intermediate spreading rate ridges. Ridge axis morphology at intermediate ridges is found to range from axial highs to axial valleys and includes morphologies that are transitional between these two end-members. Intermediate spreading ridges thus present an opportunity to examine the nature of the transition between different forms of morphology and the sensitivity of ridge structure to small changes in parameters such as spreading rates, melt supply and mantle temperature.

[5] The Southeast Indian Ridge (SEIR) is an intermediate spreading ridge (55–76 mm/yr) that displays both axial high and axial valley morphologies [*Small and Sandwell*, 1989; *Malinverno*, 1993; *Small*, 1994; *Ma and Cochran*, 1996]. In our study area, from 100°E to 112°E, spreading rate varies between 72–76 mm/yr, and the axial morphology varies from axial highs to axial valleys. These variations in morphology have been interpreted as due to changes in the magma supply (caused by variations in mantle temperature) [*Cochran et al.*, 1997; *Sempéré et al.*, 1997]. The SEIR thus presents an ideal spreading center to study the relationship between changes in shallow crustal structure and magma supply at a ridge where it appears that only mantle temperature varies along the axis. We conducted a multichannel seismic survey between 100°E–112°E to image the shallow crustal structure of the SEIR ridge axis and flanks. In this paper we investigate variations in shallow crustal structure (magma lens and layer 2A) along the SEIR axis and how changes in axial morphology, Mantle Bouguer Anomaly (MBA), ridge flank depth and abyssal hill relief relate to variations in the depth and distribution of magma lenses detected in reflection seismic data, and the thickness and geometry of seismic layer 2A. By studying the SEIR, we can assess the effects of changes in mantle temperature on crustal structure independent of chemical variation and spreading rate.

2. Tectonic Setting

[6] The SEIR is the boundary between the Australian and Antarctic plates, extending from the Rodriguez Triple Junction, located east of Madagascar at 25°S, 70°E to the Macquarie Triple Junction south of New Zealand at 63°S, 165°E. Our study area between 47°S, 100°E and 50°S, 112°E (Figure 1) is at the equator to the opening pole and as a result the spreading rate only varies by a few mm/yr through the entire region. The spreading center in this region has had a spreading rate of ~72 mm/yr since the Oligocene [*Royer and Sandwell*, 1989; *Demets et al.*, 1994].

[7] Two hot spots located to the west of our study area have been suggested to influence mantle temperature along the SEIR [*Mahoney et al.*, 2002]. Amsterdam-St. Paul is a weak near-axis hot spot located at ~77.5°–78.5°E [*Conder et al.*, 2000]. The Kerguelen and Heard hot spot group (46°S, 65°E to 64°S, 85°E) is situated approximately 1500 km south of the SEIR, but has been argued to feed material to the ridge axis near 84°E [*Small*, 1995; *Ma and Cochran*, 1996; *Yale and Phipps Morgan*, 1998].

[8] The Australian-Antarctic Discordance (AAD) (120°E–129°E) is located to the east of the study area. It is a very deep area with rough topography and a well-developed rift valley [*Palmer et al.*, 1993; *Christie et al.*, 1998] that has been interpreted as an area of cold asthenospheric conver-

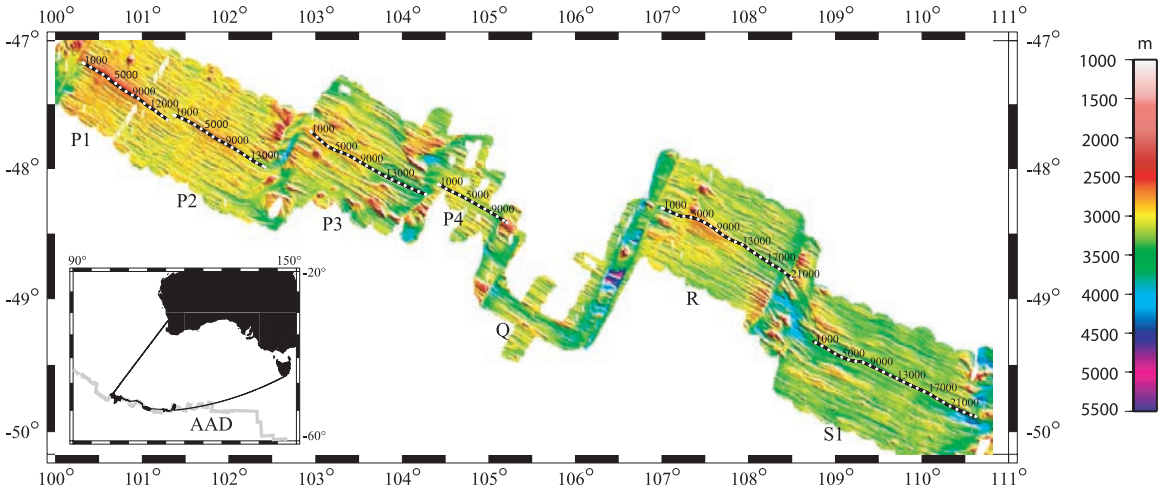

Figure 1. Shaded relief SeaBeam 2000 bathymetry map of the Southeast Indian Ridge from 100°E to 112°E with segments labeled. On-axis multichannel seismic profiles are plotted as black lines with white dots indicating every 1000th common midpoint position. The morphology of the ridge crest ranges from axial highs in the west to axial valleys in the east. Inset: Location of the study area relative to Australia, with the SEIR axis in gray and the ship track in black.

gence [*Weissel and Hayes*, 1974; *West et al.*, 1994, 1997; *Klein et al.*, 1988]. This interpretation is supported by shear wave studies that reveal faster than normal velocities indicative of a colder than normal mantle [*Forsyth et al.*, 1987]. Gravity data suggests a thin crust and low mantle temperatures within the AAD [*West et al.*, 1994]. These inferences are consistent with seismic refraction results, which indicate a crustal thickness of only 4.2 km [*Tolstoy et al.*, 1995]. Within the AAD, Fe and Si abundances suggest a shallow solidus depth, further supporting a colder mantle source [*Klein et al.*, 1991; *Pyle*, 1994]. Within the AAD, there is an isotopic boundary near 126°E interpreted as a boundary between Indian Ocean and Pacific Ocean geochemical provinces [*Klein et al.*, 1988; *Pyle*, 1994].

3. Morphology of the SEIR

[9] The segmentation of the 100°E to 112°E section of the SEIR was originally defined by *Cochran et al.* [1997] and *Sempéré et al.* [1997], and includes a series of first and second-order segments separated by transform faults, overlapping spreading centers (OSC) and propagating rifts. Although spreading rates are constant across the region, three distinct modes of axial morphology characterize the segments of the SEIR in our study area with an axial high in the west transitioning to a rifted axial high and then to a shallow axial valley to the east (Figure 2). East of 114°20′E, a deep axial valley (>1000 m) is found [*Cochran et al.*, 1997].

[10] Segment P1, the westernmost segment of our survey, centered at 101°E, has a well-defined axial high that is 15–20 km wide and 250–400 m high (Figure 2a), similar in dimension and shape to the axis of a segment of the fast spreading (90–150 mm/yr) East Pacific Rise [e.g., *Small*, 1998]. Segment P2 has a rifted axial high 15–20 km wide, but only 100–200 m high (Figure 2b). Normal faults with offsets of 50–100 m are found very close to the ridge axis, often within 1 km. Segment S1, the easternmost segment surveyed, is characterized by a shallow axial valley that is 10–15 km wide and 500–800 m deep (Figure 2c). This valley does not have a typical well-defined ''rift valley'' appearance with large bounding faults. The dimensions of the shallow axial valley along segment S1 are typical of those found along portions of other intermediate rate ridges such as the Galapagos Spreading Center (GSC) west of 95°W [*Canales et al.*, 1997, 2002; *Detrick et al.*, 2002; *Sinton et al.*, 2003].

[11] The term ''transitional'' axial morphology used previously to describe the western GSC morphology [*Canales et al.*, 1997] encompasses both what we call a rifted axial high and shallow axial valley (Figures 3d and 3e). *Christie et al.* [2005] use ''valley-and-ridge'' to describe the same range of morphologies along the eastern GSC. As we show here, rifted axial highs and shallow axial valleys are distinct morphologies, which differ in shallow axial crustal structure. Almost every individual segment along the SEIR is dominated by a

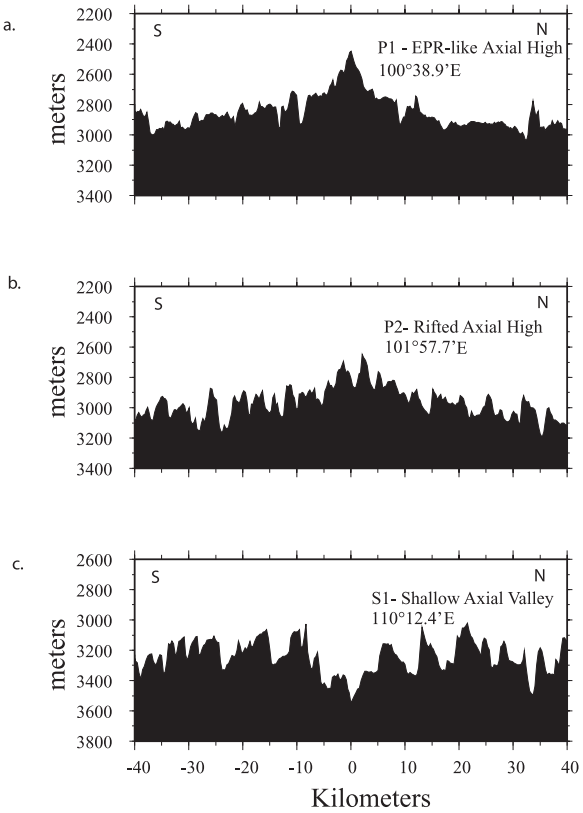

Figure 2. Cross-axis bathymetric profiles illustrating the three distinct modes of axial morphology found in our study area. Profiles are located near segment centers of (a) axial high segment P1, (b) rifted axial high segment P2, and (c) shallow axial valley segment S1. Profiles are projected parallel to the local spreading direction with longitude of axis crossing labeled. The northern flank is to the right, and the axis is at the origin of the horizontal scale.

single type of morphology, although there are two segments (Segments P3 and R) within the study area that have a transition in morphology.

[12] Within transitional segment P3, all three modes of axial morphology occur and separate the segment into three distinct subsections. To the west, there is a plateau-style axial high (102°56′E–103°13′E), with a rifted axial high in the middle section (103°13′E –103°41′E) and an axial valley further east (103°41′E–104°16′E). A transition in axial morphology is also observed in segment R (107°E –108°30′E), from a plateau axial high in the west (107°34′E to 107°46′E), to an axial valley in the east.

[13] The SEIR axis deepens by 2100 m from 88°E to116°E [*Cochran et al.*, 1997] (Figure 4d) but the change in ridge flank depth over the same distance is only 500 m (2800–3300 m) [*Ma and Cochran*, 1997] (Figure 4b). Much of the change in ridge axis depths is due to changes in the form of the dynamically supported axial morphology. In contrast, the ridge flank depth variation is isostatic in origin and provides information about along-axis changes in mantle temperature and crustal thickness [*Ma and Cochran*, 1997; *Cochran et*

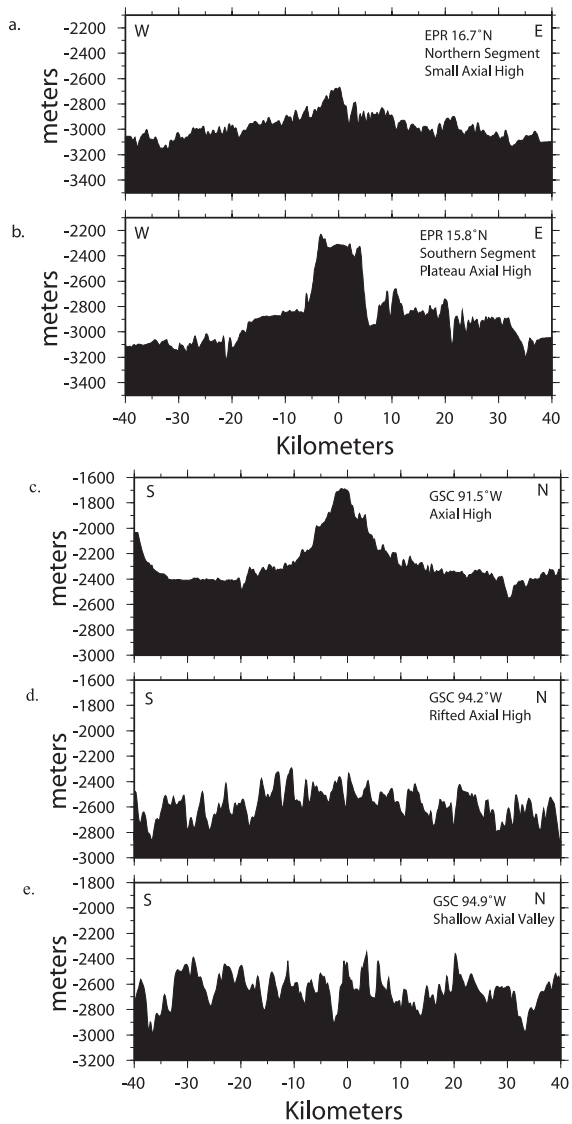

Figure 3. Bathymetric profiles across other intermediate spreading ridges at (a) EPR 16.7°N, northern, less robust segment, (b) EPR 15.8°N, southern, robust segment, (c) GSC 91.5°W, axial high, (d) GSC 94.2°W, transitional morphology, rifted axial high section, and (e) GSC 94.9°W, transitional morphology, shallow axial valley section. Profiles are projected parallel to the local spreading direction. The axis is at the origin of the horizontal scale. For the EPR profiles the eastern flank is to the right. For the GSC profiles the northern flank is to the right.

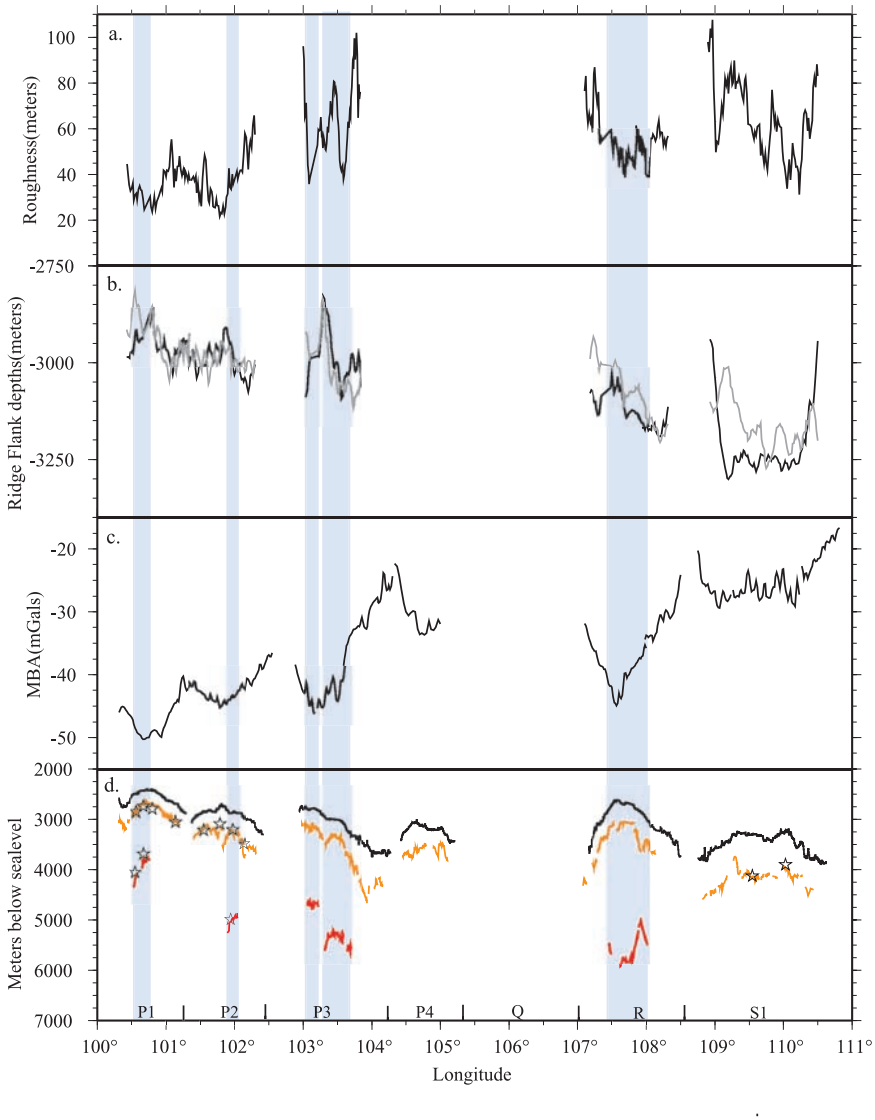

Figure 4. Along-axis profiles of ridge flank bathymetric roughness, ridge flank depths, along-axis MBA, and shallow crustal structure as a function of longitude along the SEIR. Vertical light blue boxes mark the location of the magma lenses on all profiles. (a) Bathymetric roughness [*Ma and Cochran*, 1997], representing abyssal hill relief, was determined using the EOF technique [*Small*, 1994]. Roughness lows indicating smaller abyssal hills occur midsegment and correlate with locations of the magma lenses in segments P1, P2, P3, and R. (b) Along-axis ridge flank depth at 10 km off-axis (black is the northern flank, and gray is the southern flank) [*Ma and Cochran*, 1997]. Midsegment shallow points correspond to locations of axial magma lenses (see text for discussion). (c) Axial mantle Bouguer anomaly (MBA) as a function of longitude along the SEIR [*Cochran et al.*, 1997]. Midsegment MBA lows (suggesting thicker crust or hotter mantle) correspond to locations of magma lenses along the SEIR. (d) Cross section along the axis of the SEIR showing depths to the seafloor (black), the base of layer 2A (orange), and the axial magma lens (red) reflection digitized from the along-axis multichannel seismic reflection data. Stars are measurements from cross-axis seismic lines for depth to the base of layer 2A and the magma lens.

al., 1997]. Shallower ridge flank depths can be caused by thicker crust and/or higher mantle temperatures (i.e., lower mantle density). The along-axis eastward increase in depth of the ridge flanks suggests a decrease in temperature and/or crustal thickness.

[14] Changes in axial morphology along this portion of the SEIR are accompanied by distinct changes in the form and size of abyssal hills [*Ma and Cochran*, 1996, 1997; *Goff et al.*, 1997]. *Ma and Cochran* [1997] measured bathymetric roughness on the flanks of the SEIR, which primarily

reflects abyssal hill height. They found lower bathymetric roughness (lower relief abyssal hills) associated with axial high segments and higher roughness (larger abyssal hills) at axial valley segments.

[15] A pronounced west to east regional increase in MBA gravity anomalies occurs along the SEIR from ~−65 mGals at 88°E to ~−40 mGals at 103°E at the western end of segment P3 [*Cochran et al.*, 1997] (Figure 4c). There is a sharp 10 mGal step in MBA within segment P3. To the east of this segment, axial MBA increase more gradually to −17 mGals in segment S1 at 112°E [*Cochran et al.*, 1997]. Since spreading rates and mantle source are both nearly constant along our study area [*Royer and Sandwell*, 1989; *Mahoney et al.*, 2002], *Cochran and Sempéré* [1997] and *Sempéré et al.* [1997] attribute the regional gradients in depth and gravity to a gradient in mantle temperature from hotter in the west to cooler in the east. The changes in gravity and depth between 88°E and 116°E can be explained by a west to east decrease in crustal thickness of 1.7–2.4 km, or a 55–100°C decrease in mantle temperature or some combination of the two [*Cochran et al.*, 1997].

4. Methods

[16] During December 2001 and January 2002, a multichannel seismic (MCS) survey was conducted from the R/V *Maurice Ewing* along the SEIR from 100°E to 112°E (Figure 1). The experiment consisted of detailed seismic reflection surveys with both on-axis and cross-axis (extending ~50 km away from the ridge axis) profiles within segments P1, P2, and S1. Additional on-axis seismic reflection profiles were collected along segments P3, P4, and R during transits between the main survey areas.

[17] Seismic reflection data were collected using a 6 km-long digital hydrophone streamer with 480 channels and a group spacing of 12.5 m. The seismic source was a tuned 10-gun, 3050 in^3 array that was towed at a depth of 8 m. Data were recorded at 2 ms sample rate for 12 seconds. A nominal shot interval of 50 m was used for our surveys of segments P1, P2, and P3 and a 37.5 m shot interval was used for segments P4, R and S1. The recorded signal has a bandwidth of about 2–100 Hz. The nominal common midpoint (CMP) spacing is 6.25 m and the data trace fold is 61 for segments P1, P2 and P3, and 81 for segments P4, R and S1.

[18] Extremely harsh weather conditions in the Southern Ocean resulted in a degraded signal-to-noise ratio during data acquisition, in particular during the first part of the cruise. Furthermore, poor streamer balancing also resulted in higher levels of streamer noise and significant imaging problems during surveys of segments P1 and P2.

[19] Seismic data were processed using Landmark's ProMAX seismic data processing package. Bandpass (2–7–100–125 Hz) and f-k filters on shot gathers were applied to remove cable noise and to improve signal-to-noise ratio. The data traces were then amplitude normalized, deconvolved, edited and sorted to CMP gathers. This was followed by velocity analysis, normal moveout (NMO) correction, stacking, f–k migration, and mild coherency filtering of the final reflection image. For on-axis lines semblance analysis was used to identify two-way travel time (twtt) to the magma lens reflection. Optimal stacking velocity functions for the axial profiles were constructed using the on-axis velocity solution from the East Pacific rise at 9° N [*Vera et al.*, 1990], modified for the observed travel times to the magma lens reflection and hung from the seafloor. On cross-axis lines, the on-axis velocity function was used in the axial region (1000 CMPs closest to the ridge axis). Farther off-axis, the stacking velocity function was formed using a simplified velocity function marking major velocity gradients in the crust. For the sedimented areas, the stacking velocities to the top of the igneous basement were determined using the velocity spectrum method.

[20] The base of layer 2A is marked by a velocity gradient that may correspond with the boundary between intrusives and extrusives in the oceanic crust [*Harding et al.*, 1993; *Vera and Diebold*, 1994; *Christeson et al.*, 1996]. This velocity gradient zone causes refracted or turning waves, that are recorded at far source-receiver offsets (usually >1.5 km) and can be stacked. Optimal stacking velocities for the layer 2A event are chosen from bandpass filtered (2–7–40–60 Hz) constant velocity stacks confined to the far offset traces (2–4 km), along with examination of CMP gathers. As the layer 2A event can typically be well imaged at a range of velocities, care must be taken to use consistent criteria in choosing stacking velocities. Here we selected the lowest velocities that optimize the 2A event stack. The stacked section was f–k migrated and mildly coherency filtered. A 60 ms window encompassing the 2A event was then merged into the main migrated stack section.

By using the "pick and paste" method of imaging the layer 2A arrival, the layer 2A event is optimized because the image is constrained to the far offsets where the arrival is observed [e.g., *Vera and Diebold*, 1994; *Carbotte et al.*, 2000].

[21] Two-way travel time to the layer 2A and magma lens events were converted to depth using a constant velocity of 3 km/s for layer 2A, and 5.5 km/s for the section between the base of layer 2A and the magma lens (layer 2B). These are typical crustal velocities [e.g., *Vera et al.*, 1990; *Harding et al.*, 1993; *Hooft et al.*, 1996; *Detrick et al.*, 2002] and have been confirmed through a 1-D velocity analysis (unpublished work). Uncertainties in our estimates of depth to the magma lens and layer 2A thickness arise from picking errors, and uncertainties in stacking velocities and in velocities used for depth conversion. We estimate picking errors of ±8 ms and errors due to inaccurate stacking velocities on the order of 40 ms for the layer 2A event. Considering the range of plausible interval velocities for depth conversion, we estimate uncertainties of ±80 m for magma lens depth, and ±100 m for layer 2A.

5. Results

[22] The magma lens and the base of layer 2A events were digitized for all along-axis MCS profiles. Figure 4d shows these picks, converted to meters below sea level. Figure 5 shows a map of each individual segment, with the corresponding on-axis seismic section. We report average magma lens depth and average on-axis layer 2A thickness for each segment in twtt and converted to depth using the constant velocities noted earlier, and provide the uncertainties as standard deviation. Layer 2A thicknesses for the ridge flanks are reported in twtt only.

[23] Along the axial high segment P1, a magma lens is imaged beneath ~30% of the segment at an average depth of 630 ± 50 msec twtt (~1480 m) bsf (Figures 4d and 5a). The magma lens event is confined to the shallowest, western section of the segment where it reaches the shallowest depths found in our study area. A super CMP gather from a location along segment P1 where a magma lens reflection is observed is shown in Figure 6a. From cross-axis lines, the width of the magma lens is approximately 1.1 km (Figure 7). The weak and discontinuous magma lens detected along this segment probably reflects the poor acquisition conditions discussed earlier.

[24] The average thickness of layer 2A along the axis of segment P1 is 210 ± 30 msec twtt (~310 m) and the 2A event is nearly continuous throughout the segment (Figures 4d and 5a). Layer 2A thickens away from the axis to 340 ± 60 msec twtt within 3 km of the axis (Figure 7).

[25] Along the rifted axial high segment P2, a magma lens event is observed under ~20% of the segment, at an average of 880 ± 20 msec twtt (2100 m) bsf (Figure 5b). As at segment P1, the magma lens event is only found beneath the shallowest portion of the segment. The magma lens deepens away from the segment center. From the cross-axis lines the width of the magma lens is about 1.25 km.

[26] The on-axis thickness of layer 2A at segment P2 is greater and more variable than at segment P1, with an average thickness of 310 ± 100 msec twtt (~460 m) (Figure 5b). Layer 2A is thicker beneath the eastern end of the segment where the axial high changes to a shallow axial valley approaching the transform bounding the segment (Figure 1). Off-axis, the average thickness of layer 2A determined from cross-axis lines is 340 ± 60 msec twtt, comparable to that observed on-axis and indicating minimal thickening away from the axis.

[27] A magma lens is not imaged beneath the axial valley segment P4 (Figure 5d). The base of layer 2A is well imaged beneath almost the entire segment at an average depth of 300 ± 80 msec twtt (~450 m) bsf (Figure 5d). The thickness of layer 2A varies along the segment, with the thickest layer 2A occurring in the west, and the thinnest layer 2A in the east approaching the bounding transform fault (Figure 4d).

[28] At segment S1 (110°E–112°E), the axial valley is deeper and better defined than at segment P4. No magma lens is imaged beneath this segment (Figures 4d and 5f). The layer 2A event is observed at an average twtt of 530 ± 50 msec (~800 m) bsf. However, large variations in layer 2A thickness (up to 350 m) are found along this segment. Some of the changes are gradual whereas others are abrupt. The layer 2A event is imaged along almost the entire segment, although not as a continuous event. Cross-axis lines show similar travel times to the layer 2A event off-axis as on-axis.

[29] Segment P3 is composed of three subsections each with a distinct axial morphology. Characteristics of the magma lens and layer 2A differ significantly for each subsection. Beneath the western axial plateau subsegment, a bright contin-

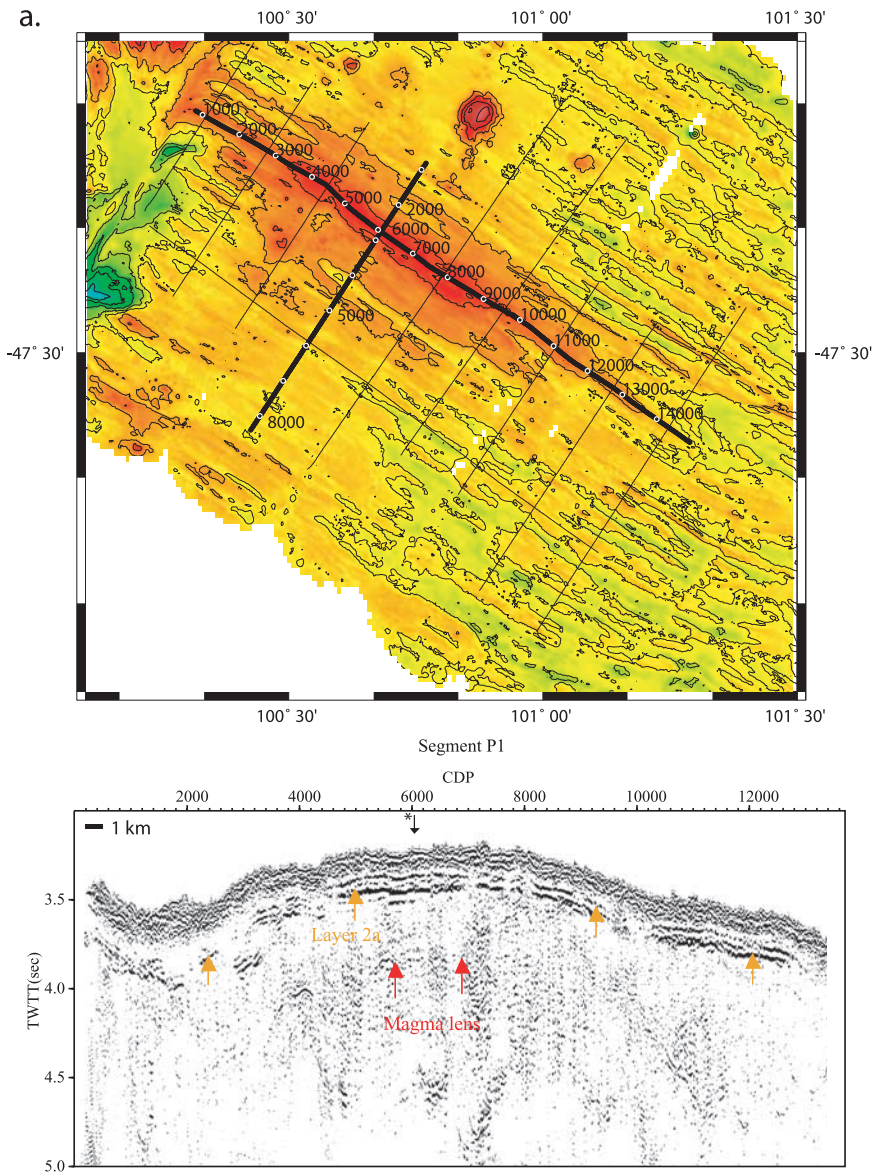

Figure 5. Bathymetric map and along-axis seismic profiles of all segments. On the maps, bold lines are profiles that are shown in this paper, and fine lines show all other survey profiles. Bold lines have a white circle every 1000th CMP. The color scale for the maps is the same as in Figure 1. On the seismic sections, arrows point to the magma lens (red) and the layer 2A events (tan). Digitized picks coincide with the white-to-black transition for the magma lens event and the black-to-white transition for the layer 2A event. Asterisks show locations of supergathers plotted in Figure 6. The black arrow on the top of the seismic section coincides with the location of the cross-axis line shown in Figure 7. (a) Segment P1 has thin nearly uniform thickness layer 2A and a shallow magma lens. (b) Segment P2 has thicker layer 2A and a deeper magma lens. (c) Segment P3 has a transition in internal crustal structure that corresponds to the transition in ridge morphology. In the westernmost part of the segment, where an axial high is observed, layer 2A is thin and the magma lens is shallow. Within the region of the rifted axial high, layer 2A is thin and the magma lens is located 600 m deeper. To the east, in the axial valley portion of the segment, layer 2A is significantly thicker and no magma lens is imaged. (d) Segment P4 has thick layer 2A with no magma lens imaged. (e) Segment R has a thick layer 2A and deep magma lens under the portion of the segment with an axial high. (f) At axial valley segment S1, layer 2A is thick and variable, and no magma lens is imaged.

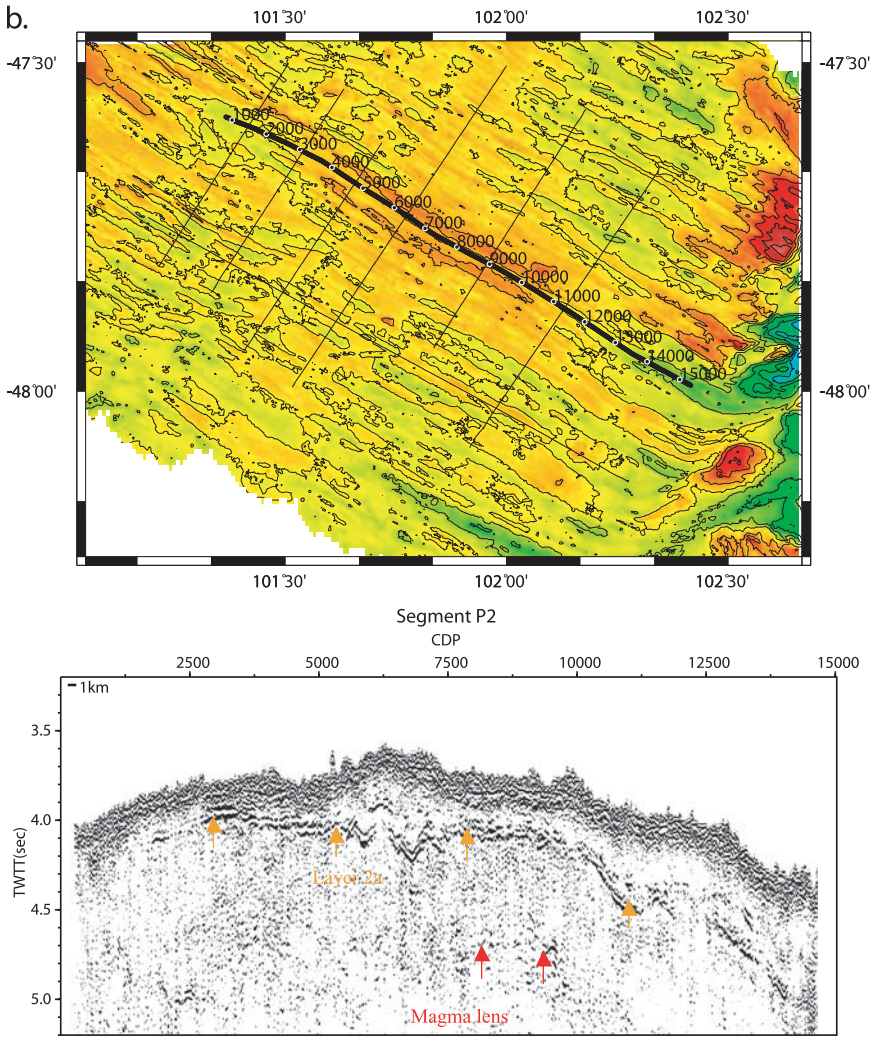

Figure 5. (continued)

uous magma lens event occurs beneath ~30% of the axis at an average depth of 810 ± 20 msec twtt (~1900 m) bsf (Figures 4d and 5b). The magma lens reflection is strong and varies little in depth.

[30] At the transition to the central, rifted axial high subsection, the magma lens abruptly drops by ~160 msec to 970 ± 40 msec twtt (~2320 m) bsf (Figures 4d and 5c). A supergather showing the magma lens event from this subsection is shown in Figure 6b. The magma lens reflector is present beneath almost the entire central subsegment with little variation in depth (Figures 4d and 5c). At the transition to the axial valley subsegment, the magma lens reflection abruptly disappears and is not imaged further east.

[31] The on-axis thickness of layer 2A also differs significantly among the subsections of segment P3. For the axial high and the rifted axial high subsections, average layer 2A thickness on axis is 250 ± 20 msec twtt (~370 m) and 270 ± 40 msec twtt (~400 m) respectively (Figures 4d and 5c). Layer 2A thickness variations are minor and the base of layer 2A is imaged as a continuous event. In contrast, in the axial valley subsection, average layer 2A thickness is 490 ± 120 msec twtt (~740 m) and the layer 2A event is discontinuous and more variable in depth.

[32] The deepest magma lens imaged in our survey is found beneath the axial high portion of segment R with an average depth of 1190 ± 90 msec twtt (~2900 m) bsf (Figures 4d and 5e). A supergather showing a weak magma lens reflection is shown in Figure 6c. No magma lens is imaged beneath the axial valley subsegment. Average layer 2A thickness along segment R is 340 ± 70 msec twtt (~510 m) (Figures 4d and 5e). The layer 2A event is detected for most of the segment and

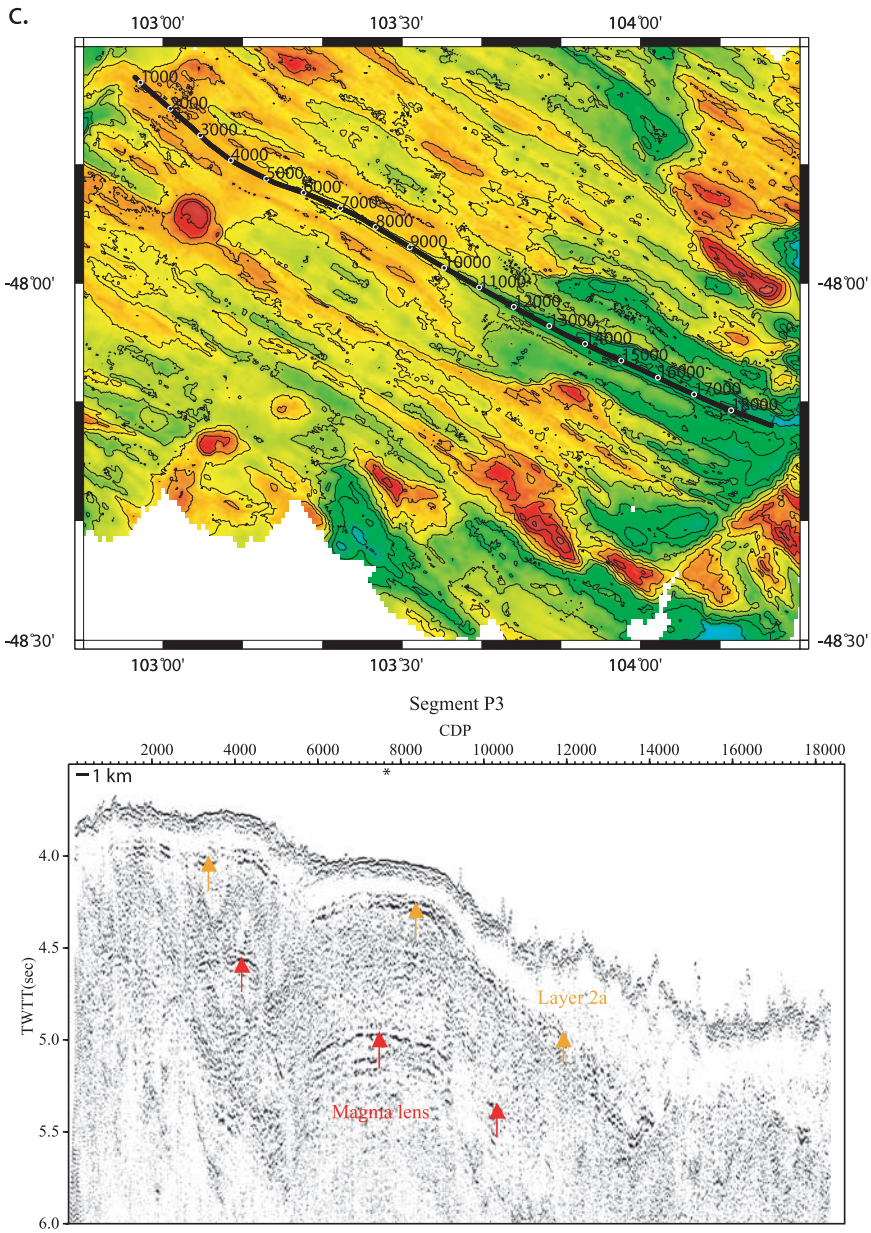

Figure 5. (continued)

varies little in depth but disappears at the easternmost end, where the axial valley becomes pronounced.

6. Discussion

6.1. Relationship Between Crustal Structure and Axial Morphology

6.1.1. Axial High

[33] Segment P1, with a well-developed 400 m "EPR-like" axial high (Figures 1 and 2), has the shallowest magma lens (~1480 m bsf) of any of the segments studied and the thinnest on-axis layer 2A (average thickness ~310 m) (Figure 4). The magma lens is ~1 km wide and present beneath ~30% of the segment (poor data acquisition conditions likely contribute to this limited extent as discussed earlier). The shallow crustal structure of segment P1 is comparable to the fast spreading EPR, where magma bodies are imaged at depths of 1200–1600 m bsf with an average width of ~725 m [*Hooft et al.*, 1997]. Thin layer 2A (200–300 m) is found on-axis at the EPR, which approximately doubles in thickness away from the axis [*Hooft et al.*, 1997].

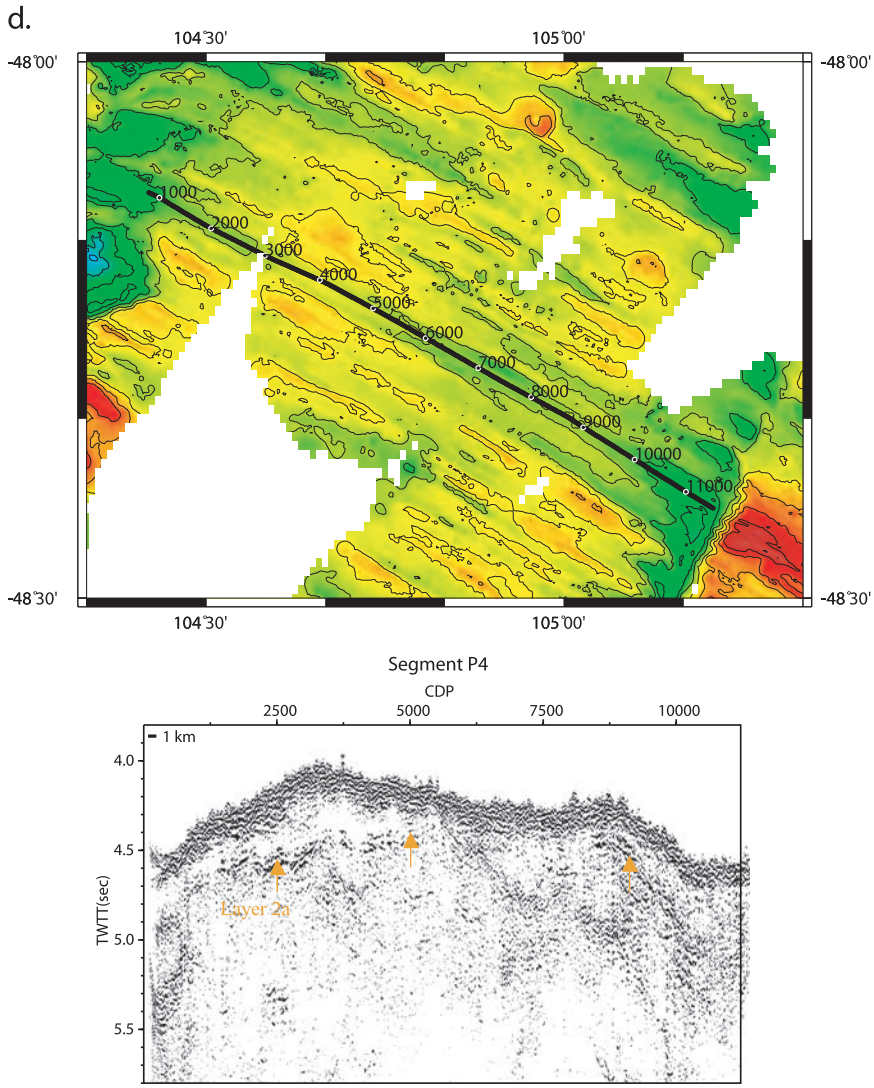

Figure 5. (continued)

6.1.2. Rifted Axial High

[34] Segment P2 has a rifted axial high morphology, which is a much more common axial morphology along intermediate spreading rate ridges [*Hooft and Detrick*, 1995; *Canales et al.*, 1997]. This segment has a deeper magma lens (average depth ~2100 m bsf) than segment P1, and thicker on-axis layer 2A (average of ~460 m) (Figure 4d). At other intermediate ridges with rifted axial highs, such as the GSC, little off-axis thickening is seen [*Blacic et al.*, 2004]. Axial highs and rifted axial highs have distinctly different shallow axial crustal structure.

6.1.3. Axial Valleys

[35] Axial valleys characterize segments P4 and S1. A magma lens is not imaged at either of these segments, and layer 2A is thicker on-axis than at segment P1 (P4: ~450 m, S1: ~800 m) (Figure 4d). Large variations in on-axis layer 2A thickness are found along segment S1. Although we cannot completely rule out imaging limitations due to, for example, the rough axial topography, our data indicate a direct relationship between the presence or absence of a magma lens reflector and axial morphology. Along the SEIR, segments with a magma lens have an axial high and segments without a magma lens have an axial valley.

6.1.4. Transitional Segments

[36] Transitions in morphology from an axial high to axial valley occur in segments P3 and R. As discussed earlier, segment P3 is composed of three subsections, with an axial high section in the west, a rifted axial high in the center and an axial valley section in the east. Changes in axial morphology

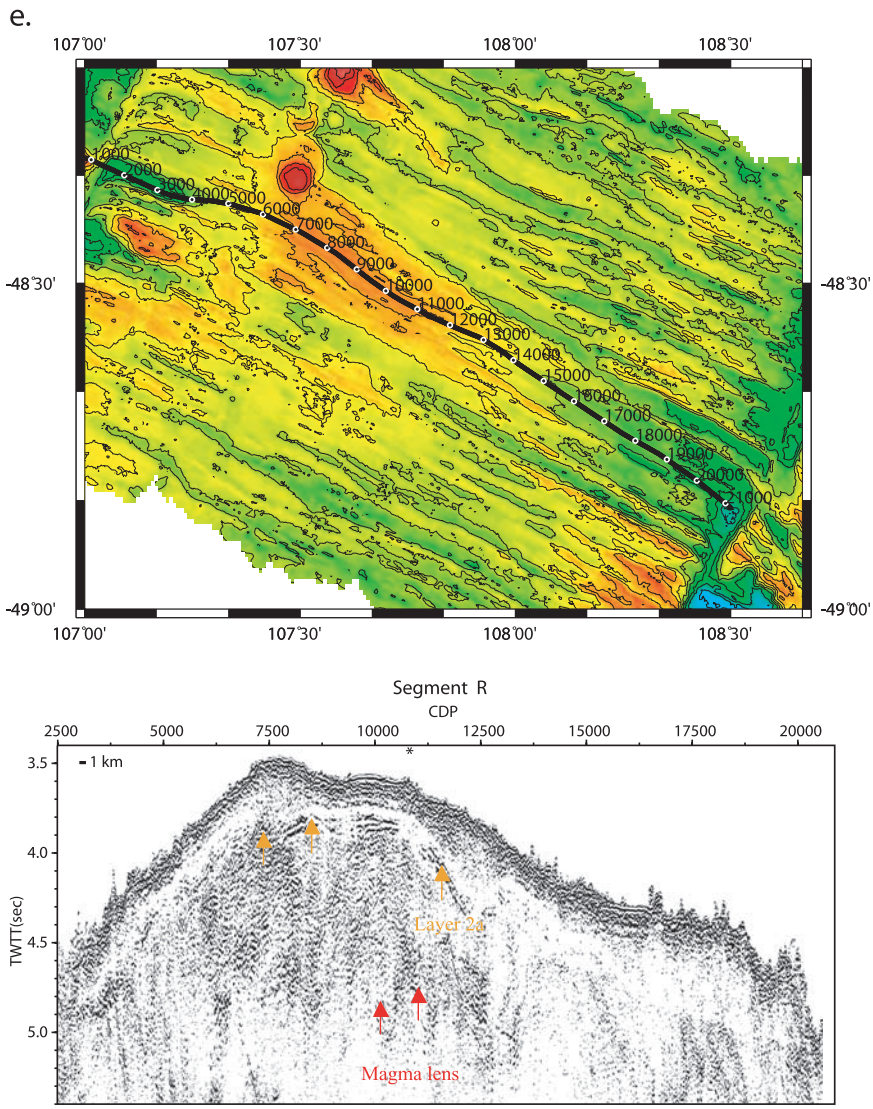

Figure 5. (continued)

are abrupt and coincide with minor third- or fourth-order segment boundaries [*Cochran and Sempere*, 1995]. The melt lens drops abruptly from 1900 m bsf to 2320 m bsf coincident with the boundary between the axial high and rifted axial high subsections (Figures 4d and 5c). No melt lens is imaged in the axial valley subsegment. The average on-axis thickness of layer 2A also increases from ~370 m along the axial high and rifted axial high portions of the segment to ~740 m in the axial valley subsegment. These abrupt transitions in axial morphology with corresponding abrupt changes in the depth/presence of the magma lens reflection and in layer 2A thickness suggest that these are distinct modes of crustal accretion.

[37] Along this section of the SEIR, the ridge flank depths vary slowly and smoothly. Ridge flank depths on the swath bathymetry profiles across Segment P4 with a shallow axial valley are only about 50 m deeper than the average ridge flank depths in Segment P2 with a rifted axial high. This small change in depth suggests that the change in axial morphology does not result from a large change in mantle temperature, but rather is a threshold-type response to a gradual increase in mantle temperature to the west.

[38] Segment P3 also marks a regional transition in ridge structure along the SEIR. Segments to the west of P3 consistently have axial highs (either rifted or EPR-like) whereas axial valleys are found along almost all segments east of P3 through to the AAD (the single exception, segment R, is discussed below). The segregation of axial highs to the west of segment P3 and axial valleys to the east

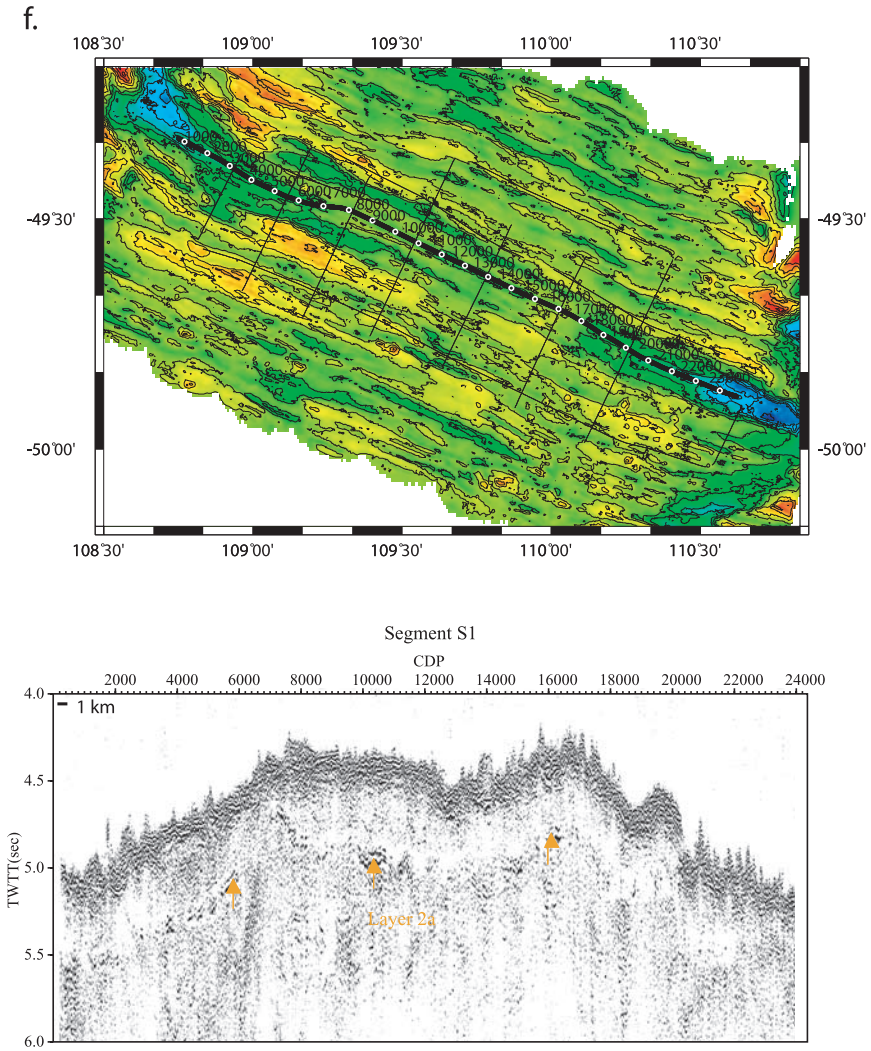

Figure 5. (continued)

of the segment supports the hypothesis that at a constant spreading rate, the axial morphology depends on the mantle temperature. The rapid transitions in axial morphology within P3 coinciding with the disappearance of a detectable magma lens suggest that there is a threshold-type trigger for these related changes in axial morphology and shallow crustal structure.

[39] Anomalous segment R, located east of the regional transition to axial valley morphology, has an axial high along its western portion. Average abyssal hill relief for the entire segment is high and comparable to that observed within the adjacent axial valley segments [*Ma and Cochran*, 1997]. Though the morphology of the western part of segment R is similar to that of segment P1, the magma lens imaged beneath this region lies much deeper in the crust (by ~1400 m). Cooler mantle temperatures for segment R are inferred from the regional gravity and ridge flank depth gradients, possibly accounting for a magma lens that resides deeper in the crust. The thickness of layer 2A on-axis is also greater here than at P1, and falls within the range observed for axial valley segments. As discussed below, segment R is a leading ridge segment in the absolute plate motion reference frame, and the anomalous nature of this segment may reflect enhanced magma delivery due to the ridge migration effect proposed by *Carbotte et al.* [2004].

[40] Abrupt transitions in ridge crest morphology with coincident changes in crustal structure have been found at other intermediate spreading ridges. Along the fast-intermediate (85 mm/yr) spreading EPR north of the Orozco transform, a shallow magma lens (1470 m bsf) and thin layer 2A (160 m) are detected beneath the shallow and broad axial high of the southern segment centered at 15.7°N (Figures 3a and 3b) [*Carbotte et al.*,

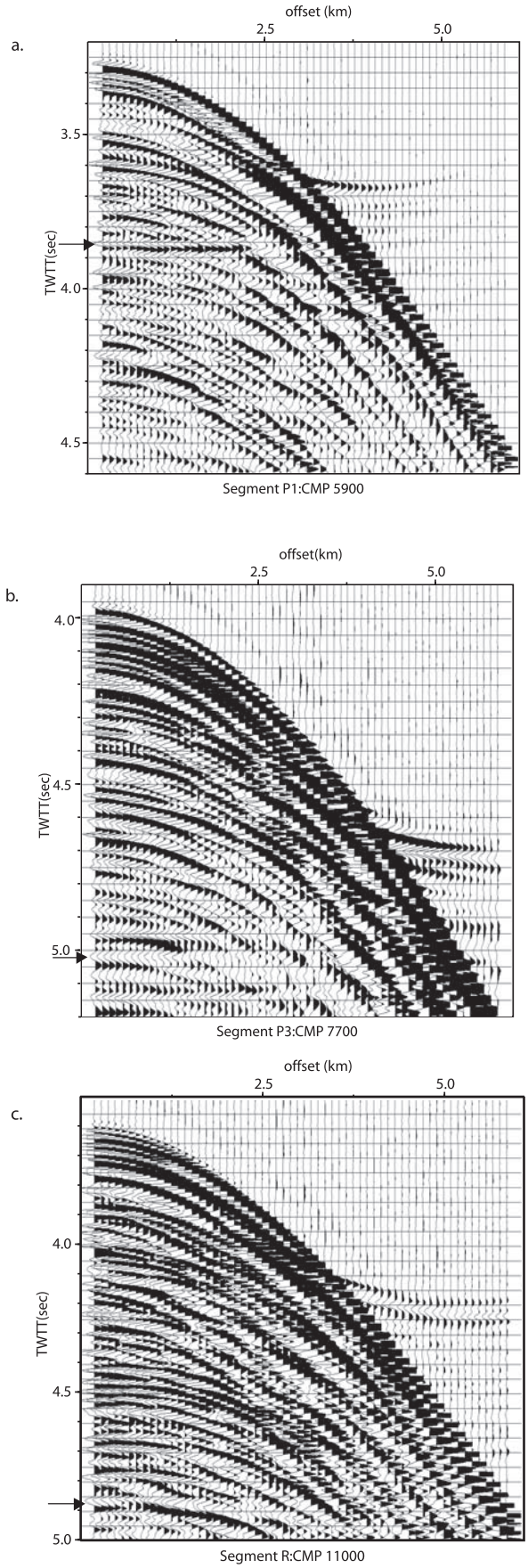

1998]. In contrast a deeper magma lens (1750 m bsf) and thicker 2A (260 m) are found beneath the narrow and deeper axis of the adjoining segment to the north (Figures 3a and 3b). Along the western GSC, axial morphology changes from an axial high in the east, to rifted axial high, to shallow axial valley and then to an axial valley in the west away from the Galapagos hot spot. The transition from axial high to rifted axial high morphology along the GSC occurs at 92°38′W [*Sinton et al.*, 2003] and coincides with an abrupt increase in magma lens depth from 1.5–2.5 km to 2.5–4.25 km, along with a thickening of layer 2A from 150–350 m to 300–500 m [*Detrick et al.*, 2002]. The inflated western GSC thus shares the same properties as the SEIR in terms of variations in the depth/presence of a magma lens and thickness of layer 2A with changes in axial morphology.

[41] The underlying cause of changes in magma supply at these ridges may differ, although the abrupt transitions in ridge structure that result are similar. At 16°N on the EPR, a linear seamount chain extends west of the shallow and broad southern segment, and the inflated ridge morphology and shallow magma lens observed here are attributed to enhanced magma supply due to tapping of the magmatic source for the seamount chain [*Carbotte et al.*, 2000]. Along the GSC, variations in magma supply with distance from the Galapagos hot spot and with changes in spreading rate may both contribute to the observed changes in shallow crustal structure with the influence of these factors difficult to distinguish [*Detrick et al.*, 2002]. Along the SEIR, spreading rate is constant and changes in ridge morphology appear to be related to along-axis changes in mantle temperature causing changes in magma supply to the crust [*Cochran et al.*, 1997; *Sempéré et al.*, 1997]. The trigger for changes in ridge structure may differ in different tectonic settings, but the transition is consistently abrupt indicating a threshold type response.

6.2. Relationship Between Magma Supply and Axial Morphology

[42] *Purdy et al.* [1992] suggested a systematic relationship between magma chamber depth and

Figure 6. On-axis CMP supergather stacks (96 gathers) (a) P1 (CMP 5900-5995), (b) P3 (CMP 7700–7795), and (c) R (11000–11095). Gathers are NMO corrected to an appropriate velocity (P1: 2.3 km/sec, P3: 2.6 km/sec, R: 2.4 km/sec) to flatten the magma lens arrival, noted by arrows.

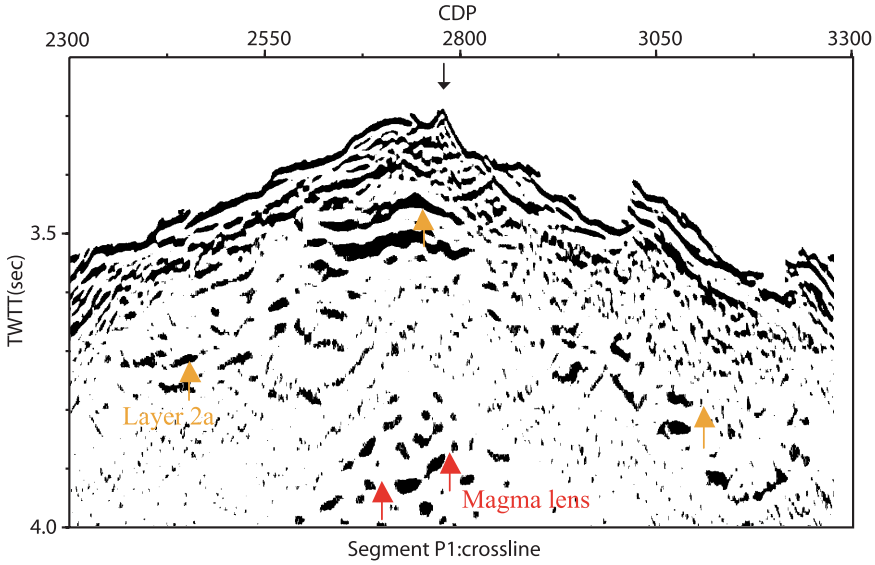

Figure 7. Cross-axis profile for segment P1 (see Figure 5a for location of the line). Thickening of layer 2A off-axis is clearly seen in segment P1. The magma lens is also imaged. The length of the section shown is 6250 m.

spreading rate, with faster spreading rate ridges having shallow magma lenses, and slower spreading rate ridges having deeper magma lenses. Figure 8a shows AMC depths plotted as a function of spreading rate redrawn from *Carbotte et al.* [1998] with our data from the SEIR included. In this figure we distinguish data from axial high (blue oval) and rifted axial high (green oval) segments. Also shown is the predicted depth to the magma lens reflector (salmon-colored curve), assumed to be the freezing horizon for melts, with the assumption of a 6 km-thick crust from *Phipps Morgan and Chen* [1993]. The Phipps Morgan and Chen model predicts a rapid increase in the depth to the magma lens reflector at intermediate rates, as is generally observed. Depth to the magma lens for segments with well-developed axial highs decreases slowly with decreasing spreading rate. Along the Reykjanes Ridge, a well-developed axial high and a shallow magma body are observed [*Sinha et al.*, 1997] despite slow spreading rates. At rifted axial high segments, depth to the magma lens reflector increases rapidly with decreasing spreading rate and rifted axial highs have not been mapped at spreading rates less than ~45 mm/yr (Figure 8a). Individual segments of the SEIR fit with these global mid-ocean ridge trends. Both the axial high and the rifted axial high segments of the SEIR and GSC occur at a range of depths, comparable to other mid-ocean ridges. Segment R plots within the rifted axial high field reflecting its transition in morphology. On the other hand, P3 has distinctly different subsegments, including an axial high and rifted axial high subsegment that plot within the ranges observed elsewhere for these morphologies.

[43] The on-axis thickness of layer 2A also varies with axial morphology (Figure 8b). At axial high segments at both fast and intermediate spreading ridges, layer 2A is thin on-axis. For segments with an axial valley or a rifted axial high, layer 2A is thicker and/or more variable in thickness on-axis. This difference is most likely due to the presence of inward-facing faults near the axis at ridges axes with rifted highs or axial valleys. These faults prevent flow of magma downhill away from the axis, so layer 2A reaches its full thickness on-axis.

6.3. Steady State Nature of Accretion Along the SEIR

[44] Along the SEIR we find an excellent correlation between the location of magma lenses and MBA gravity lows at the axis, shallower depths on the ridge flanks, and lower bathymetric roughness for crust up to 1 m.y. in age (Figure 4). Both the MCS image and the MBA gravity give a picture of crustal and mantle structure at the present time, whereas ridge flank depths and bathymetric roughness reflect crustal accretion conditions in the past. The correlation of ridge axis properties with ridge flank properties suggest that patterns of accretion along the SEIR are steady state; that locations of vigorous mantle supply of melt have not changed with time over the past 1 m.y.

[45] In all four of the segments (P1, P2, P3, and R) in which magma lenses are detected, a MBA gravity low coincides with the location of the magma lens (Figure 4). MBA lows are commonly interpreted as caused by thicker crust and/or the presence of hotter mantle [e.g., *Kuo and Forsyth*, 1988; *Lin et al.*, 1990; *Wang and Cochran*, 1993; *Detrick et al.*, 1995]. The MBA lows observed along the SEIR are associated with the presence of an axial magma lens and shallow axial depth consistent with enhanced supply of melt from the mantle at these locations.

[46] Ridge flank depths measured by *Ma and Cochran* [1997] show local shallow regions within each segment, superimposed on the regional increase in depths to the east that mimics the ridge axis trend (Figure 4). Flank depths are measured in this study at 10 km from the ridge axis, which corresponds with crustal ages of 260,000 years. Whereas the large changes in axial depth must reflect, in part, dynamic support of the ridge axis morphology, the depth changes on the ridge flanks are assumed to be isostatically supported, reflecting variations in crustal thickness. *Ma and Cochran* [1997] attribute the shallower off-axis areas to slightly thicker crust reflecting locally enhanced melt supply when formed. The regions of shallowest ridge flank depth within segments P1, P2, and

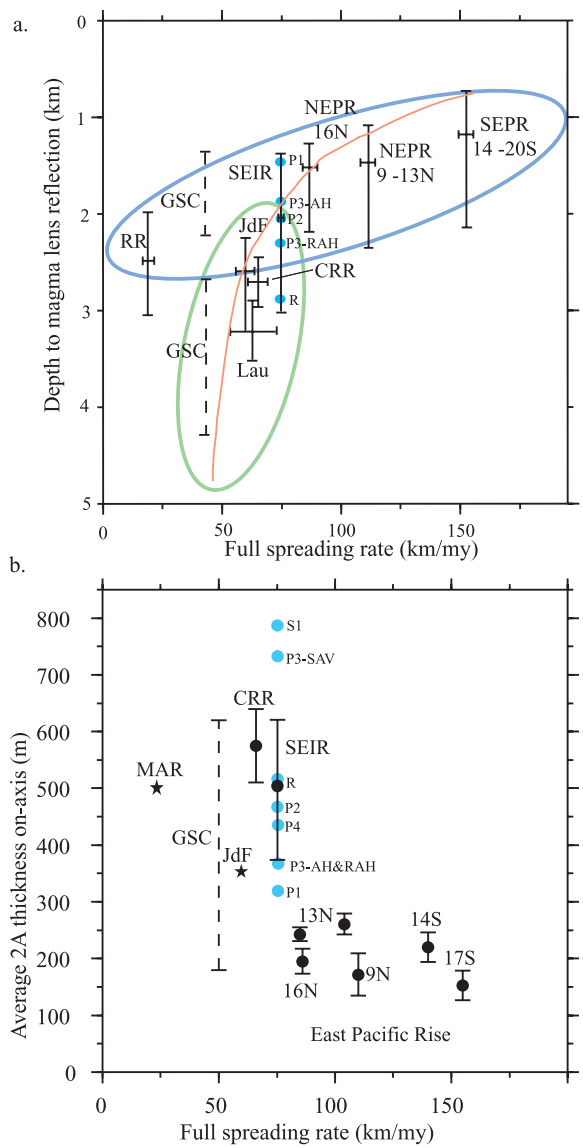

Figure 8. (a) Average depth to the magma lens with spreading rate. The salmon curve is the 1200°C isotherm calculated from the ridge thermal model of *Phipps Morgan and Chen* [1993]. Ellipses represent axial high (blue) and rifted axial high (green) morphologies and suggest a different range of magma lens depths dependent on axial morphology. Axial highs have a small range of shallow depths for the magma lens, and rifted axial highs have a deeper magma lens that increases rapidly in depth with decreasing spreading rate. Ridges included are Reykjanes Ridge (RR) [*Sinha et al.*, 1997], Juan de Fuca Ridge (JdF) [*Morton et al.*, 1987], Costa Rica Rift (CRR) [*Mutter et al.*, 1995], Lau Basin (Lau) [*Collier and Sinha*, 1990], Northern and Southern East Pacific Rise (NEPR, and SEPR) [*Detrick et al.*, 1987; *Purdy et al.*, 1992; *Carbotte et al.*, 1998], Galapagos Spreading Center (GSC) [*Detrick et al.*, 2002], and Southeast Indian Ridge (SEIR) (this paper). The SEIR data are also plotted in turquoise dots, representing the average depth to the magma lens for each segment. Adapted from *Carbotte et al.* [1998]. (b) Thickness of layer 2A as a function of spreading rate measured on-axis. Results from seismic reflection surveys coincide with black dots at average values with standard deviation (solid lines) or as a range (dashed lines) where no standard deviations are available. Filled stars correspond with results from wide-angle reflection and refraction data. On-axis layer 2A is generally relatively thin (<300 m) at high spreading rates. At spreading rates <75 mm/yr, there is significantly greater scatter, and the thickness tends to be greater. Sources are East Pacific Rise (EPR): 16°N, *Carbotte et al.* [2000]; 13°N, *Babcock et al.* [1998]; 9°N, *Harding et al.* [1993] and *Kent et al.* [1993a, 1993b]; 14°S *Kent et al.* [1994] and *Hooft et al.* [1997]; and 17°S *Carbotte et al.* [1997] and *Hooft et al.* [1997]. Galapagos Spreading Center (GSC): *Detrick et al.* [2002] (twtt converted to depth using an assumed velocity of 2.5 km/sec. Costa Rica Rift (CRR): *Buck et al.* [1997] and *Floyd et al.* [2002]. Juan de Fuca Ridge (JdF): *Rohr* [1994] and *McDonald et al.* [1994] and *Morton et al.* [1987] (filled stars). Mid-Atlantic Ridge (MAR): *Hussenoeder et al.* [2002]. SEIR (this paper) with each segment average layer 2A thickness plotted in turquoise dots. Adapted from *Carbotte* [2001].

P3 coincide with on-axis MBA lows, and magma lens location (Figure 4) supporting the idea of a long-lived enhanced melt supply in these particular locations.

[47] In their analysis of bathymetric roughness on the flanks of the SEIR, *Ma and Cochran* [1997] found v-shaped lows in roughness roughly centered on segment midpoints (Figure 4a, Segments P1, P2 and R). They attributed these regions of lower abyssal hill relief to weaker axial lithosphere resulting in smaller throw faults. They further speculated that each of these roughness lows might be associated with a melt body on-axis. Our work indicates that each of the bathymetric roughness minima in segments P1, P2 and R does indeed coincide with the location of a melt lens on-axis. Remarkably, two roughness minima are observed in segment P3 that coincide with the two western subsegments of P3, both of which have an axial magma lens. The roughness estimates in *Ma and Cochran* [1997] are averaged over 40 km perpendicular to the axis, representing over 1 million years. The persistence of the bathymetric roughness minima at the same location over 1 m.y. suggests that the magmatic centers of these segments have remained constant over this time.

6.4. Local Controls on Melt Supply Along the SEIR

[48] The large-scale regional changes in ridge axis depth and morphology observed along the SEIR are associated with a west to east decrease in mantle temperature approaching the AAD inferred from axial gravity data with presumed changes in magma supply to the crust [e.g., *Cochran et al.*, 1997; *Sempéré et al.*, 1997]. Superimposed on this long wavelength trend are local, shorter-wavelength, variations in axial depth and morphology. These inter-segment variations may reflect local differences in magma supply to ridge segments associated with the ridge migration effect proposed by *Carbotte et al.* [2004]. From a study of changes in axial depth across ridge-axis discontinuities, *Carbotte et al.* [2004] find that ridge segments offset in the direction of ridge migration over the deep mantle (termed "leading" segments) are typically the shallower and morphologically robust segments. *Carbotte et al.* [2004] propose that asymmetric mantle upwelling and melt production due to ridge migration combined with 3D melt tapping from this asymmetric melt production zone, may account for these observations. In their model, magma supply to leading segments across a discontinuity is enhanced by preferential entrainment of melts from the faster upwelling, more melt rich mantle beneath an advancing plate.

[49] The SEIR is migrating to the northeast in the absolute motion reference frame (Figure 9) [e.g., *Small and Danyushevsky*, 2003]. Hence leading segments across discontinuities of this ridge are those that are offset to the north (i.e., P3, R) (Figure 9). Within our study area, axial highs are found preferentially along leading segments and in most cases leading segments are shallower than adjacent trailing segments (Figure 9). Additionally, magma bodies in the crust are found preferentially at leading segments. Beneath leading segment P3, a bright continuous magma lens is found at the northwestern end of the segment, reaching shallower depths in the crust than the isolated magma lens detected beneath adjacent trailing segment P2. All segments east of P3 display axial valleys, except for segment R, which is also a leading segment (Figure 9). A deep magma lens is found beneath the axial high portion of this segment, whereas there is no evidence for magma in the crust beneath the adjacent trailing segment S1. These observations support the notion that magma supply to leading segments is enhanced and are consistent with predictions of the ridge migration model for segment-scale variations in magma supply.

7. Conclusions

[50] 1. Along the SEIR, axial morphology is directly related to shallow crustal structure, suggesting distinct modes of crustal accretion. Axial highs along the SEIR have shallow magma lenses, and thin on-axis layer 2A. Rifted axial highs have deeper magma lenses, and thicker on-axis layer 2A. Magma lenses are not detected beneath segments with axial valleys, and layer 2A is thick on-axis.

[51] 2. Changes in axial morphology along the SEIR are abrupt, suggesting a small change in mantle temperature causes a large change in crustal structure. Abrupt changes in axial morphology are also seen between segments at other ridges.

[52] 3. Current variations in axial crustal structure along the SEIR appear to persist through time, at least for the past 1 m.y. Locations of magma lenses along axis correspond to MBA gravity lows as well as off-axis features of shallower ridge flank depths, and lower relief abyssal hills. It appears that magma lenses have existed in the same location for at least the last ~250,000 years and probably

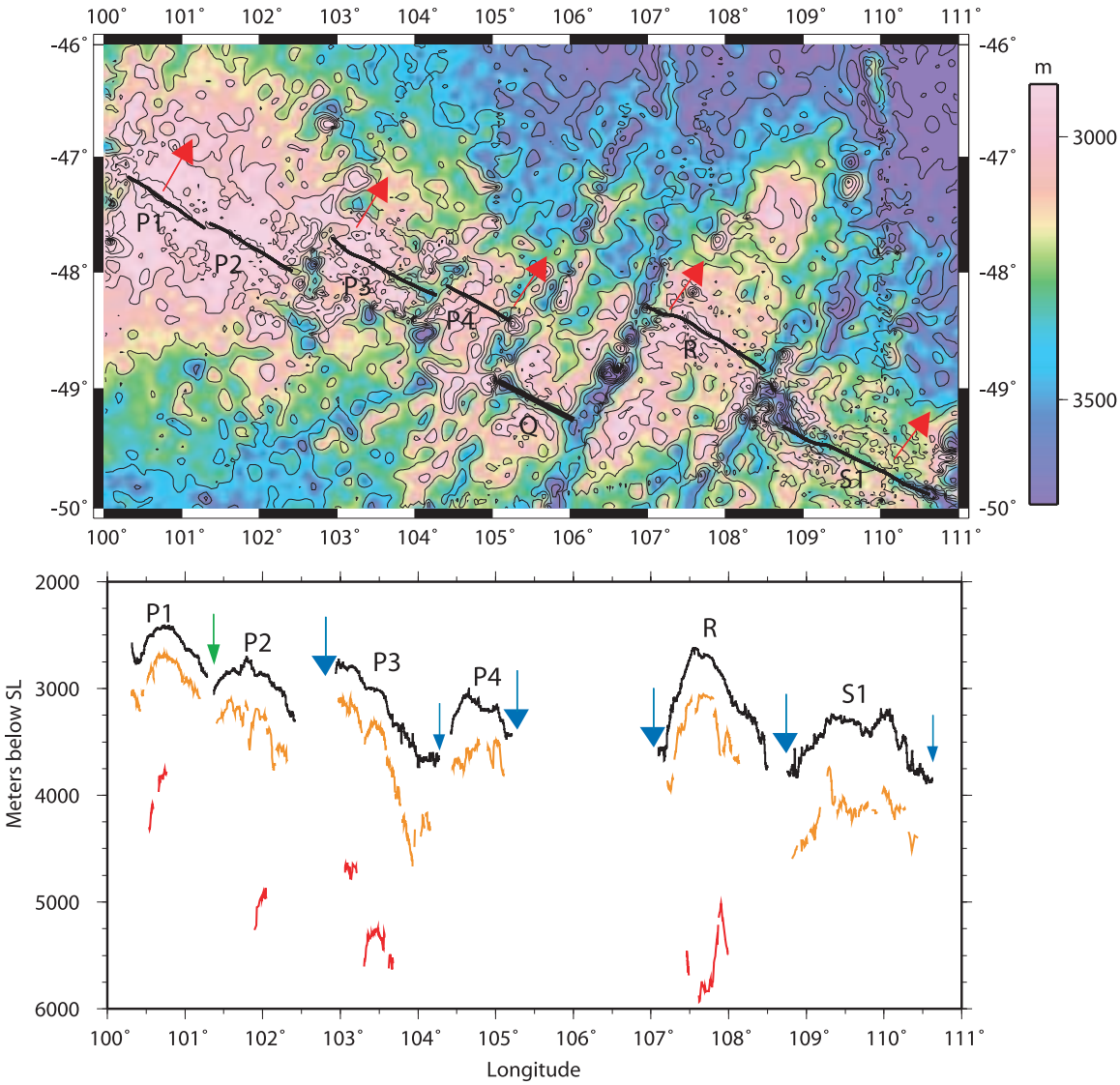

Figure 9. (a) Overview map of the SEIR with the ridge axis in black. Red arrows indicate the direction of ridge axis migration (45–46 mm/yr) calculated from *Gripp and Gordon* [1990]. (b) Digitized cross section of the SEIR with the seafloor in black, layer 2A in orange, and the magma lens in red. Blue arrows indicate where the leading segment across a discontinuity is shallower than the trailing segment. Green arrow indicates where the trailing segment is shallower than the leading segments. Large arrows are transform faults, and small arrows are second-order offsets.

for the past 1 million years, suggesting that the SEIR is in steady state.

[53] 4. In the global system, magma supply controls ridge morphology and crustal structure at a given spreading rate. Axial highs, over a wide range of spreading rates, have a limited range of depths to magma lens ranging from 1 km to 2.25 km. Rifted axial highs occur only at intermediate spreading rates and have a range of magma lens depths of 2.5–4 km. No magma lens has been imaged to date beneath ridge axes with an axial valley.

[54] 5. Regional changes in ridge morphology are attributed to a long wavelength gradient in mantle temperature beneath the SEIR, with axial high segments found where warmer mantle is inferred, and axial valleys located where the mantle is cooler. Superimposed on this regional trend are intersegment variations consistent with variable magma supply associated with ridge migration. Within both the axial high and axial valley dominated portions of the SEIR, leading segments are preferentially associated with an axial high morphology, shallower axis depths, and detectable magma bodies in the crust.

Acknowledgments

[55] This work was supported by National Science Foundation grant 99-11720. We would like to thank Captain Mark Landow and the officers, crew, and scientific staff of R/V *Maurice Ewing* for their assistance under often extremely difficult weather and sea conditions. We thank David Christie and an anonymous reviewer for their helpful comments. J.M.B. thanks M.S., A.G., and J.P.S. The GMT software package [*Wessel and Smith*, 1998] was used extensively in the preparation of figures. This is LDEO contribution 6824.

References

Babcock, J. M., A. J. Harding, G. M. Kent, and J. A. Orcutt (1998), An examination of along-axis variation of magma chamber width and crustal structure on the East Pacific Rise between 13°30′N and 12°20′N, *J. Geophys. Res.*, *103*(B12), 30,451–30,468.

Blacic, T. M., G. Ito, J. P. Canales, R. S. Detrick, and J. Sinton (2004), Constructing the crust along the Galapagos Spreading Center 91.3°–95.5°W: Correlation of seismic layer 2A with axial magma lens and topographic characteristics, *J. Geophys. Res.*, *109*, B10310, doi:10.1029/2004JB003066.

Buck, W. R., S. M. Carbotte, and C. Z. Mutter (1997), Controls on extrusion at mid-ocean ridges, *Geology*, *25*, 935–938.

Calvert, A. J. (1995), Seismic evidence for a magma chamber beneath the slow-spreading Mid-Atlantic Ridge, *Nature*, *377*(6548), 410–414.

Calvert, A. J. (1997), Backscattered coherent noise and seismic reflection imaging of the oceanic crust: An example from the rift valley of the Mid-Atlantic Ridge at 23°N, *J. Geophys. Res.*, *102*(B3), 5119–5134.

Canales, J. P., J. J. Dañobeitia, R. S. Detrick, E. E. E. Hooft, R. Bartolomé, and D. F. Naar (1997), Variations in axial morphology along the Galápagos spreading center and the influence of the Galápagos hotspot, *J. Geophys. Res.*, *102*(B12), 27,341–27,354.

Canales, J. P., J. A. Collins, J. Escartín, and R. S. Detrick (2000), Seismic structure across the rift valley of the Mid-Atlantic Ridge at 23°20′ (MARK area): Implications for crustal accretion processes at slow spreading ridges, *J. Geophys. Res.*, *105*(B12), 28,411–28,426.

Canales, J. P., G. Ito, R. S. Detrick, and J. Sinton (2002), Crustal thickness along the western Galapagos Spreading Center and the compensation of the Galapagos hotspot swell, *Earth Planet. Sci. Lett*, *203*, 311–327.

Carbotte, S. M. (2001), Mid-ocean ridge seismic structure, in *Encyclopedia of Ocean Sciences*, pp. 1788–1798, Elsevier, New York.

Carbotte, S. M., J. C. Mutter, and L. Xu (1997), Contribution of volcanism and tectonism to axial and flank morphology of the southern East Pacific Rise, 17°10′-17°40′S, from a study of layer 2A geometry, *J. Geophys. Res.*, *102*(B5), 10,165–10,184.

Carbotte, S. M., C. Z. Mutter, J. Mutter, and L. Wu (1998), Insights from a fast-intermediate spreading ridge on the influence of magma supply and spreading rate on crustal magma bodies and emplacement of the extrusive layer, *Geology*, *26*, 455–458.

Carbotte, S. M., A. Solomon, and G. Ponce-Correa (2000), Evaluation of morphological indicators of magma supply and segmentation from a seismic reflection study of the East Pacific Rise at 15°30′-17°N, *J. Geophys. Res.*, *105*, 2737–2759.

Carbotte, S. M., C. Small, and K. Donnelly (2004), The influence of ridge migration of the magmatic segmentation of mid-ocean ridges, *Nature*, *429*, 743–746.

Christeson, G. L., G. M. Kent, G. M. Purdy, and R. S. Detrick (1996), Extrusive thickness variability at the East Pacific Rise, 9°–10°N: Constraints from seismic techniques, *J. Geophys. Res.*, *101*, 2859–2873.

Christie, D. M., B. P. West, D. G. Pyle, and B. B. Hanan (1998), Chaotic topography, mantle flow and mantle migration in the Australian-Antarctic discordance, *Nature*, *394*, 637–644.

Christie, D. M., R. Werner, F. Hauff, K. Hoernle, and B. B. Hanan (2005), Morphological and geochemical variations along the eastern Galápagos Spreading Center, *Geochem. Geophys. Geosyst.*, *6*, Q01006, doi:10.1029/2004GC000714.

Cochran, J. R., and J. C. Sempere (1995), *Cruise Report: Geophysical Study of the Southeast Indian Ridge Between 90° and 120° E West 09MV Fremantle (Australia) - Fremantle (Australia), December 10, 1994–January 23, 1995*, 89 pp., Columbia Univ., New York.

Cochran J. R., J. Sempéré, and SEIR Scientific Team (1997), The Southeast Indian Ridge between 88°E and 118°E: Gravity anomalies and crustal accretion at intermediate spreading rates, *J. Geophys. Res.*, *102*(B7), 15,463–15,487.

Collier, J., and M. C. Sinha (1990), Seismic images of a magma chamber beneath the Lau Basin back-arc spreading center, *Nature*, *346*(6285), 646–648.

Conder, J. A., D. S. Scheirer, and D. W. Forsyth (2000), Seafloor spreading on the Amsterdam-St. Paul hotspot plateau, *J. Geophys. Res.*, *105*, 8263–8277.

DeMets, C., R. G. Gordon, D. F. Argus, and S. Stein (1994), Effect of recent revisions to the geomagnetic reversal time scale on estimates of current plate motions, *Geophys. Res. Lett.*, *21*, 2191–2194.

Detrick, R. S., P. Buhl, E. E. Vera, J. C. Mutter, J. A. Orcutt, J. A. Madsen, and T. M. Brocher (1987), Multichannel seismic imaging of the axial magma chamber along the East Pacific Rise between 9°N and 13°N, *Nature*, *326*, 35–41.

Detrick, R. S., J. C. Mutter, P. Buhl, and I. I. Kim (1990), No evidence from multichannel reflection data for a crustal magma chamber in the MARK area on the Mid-Atlantic Ridge, *Nature*, *347*, 61–64.

Detrick, R. S., A. J. Harding, G. M. Kent, J. A. Orcutt, J. C. Mutter, and P. Buhl (1993), Seismic structure of the southern East Pacific Rise, *Science*, *259*, 499–503.

Detrick, R. S., H. D. Needham, and V. Renard (1995), Gravity anomalies and crustal thickness variations along the Mid-Atlantic Ridge between 33°N and 40°N, *J. Geophys. Res.*, *100*, 3767–3787.

Detrick, R. S., J. M. Sinton, G. Ito, J. P. Canales, M. Behn, T. Blacic, B. Cushman, J. E. Dixon, D. W. Graham, and J. J. Mahoney (2002), Correlated geophysical, geochemical, and volcanological manifestations of plume-ridge interaction along the Galápagos Spreading Center, *Geochem. Geophys. Geosyst.*, *3*(10), 8501, doi:10.1029/2002GC000350.

Floyd, J. S., J. C. Mutter, and S. M. Carbotte (2002), Seismic reflection imaging of the evolution of oceanic crustal structure at the intermediate rate spreading Costa Rica Rift, *Eos Trans. AGU*, *83*(47), Fall Meet. Suppl., Abstract T12B-1318.

Forsyth, D. W., R. L. Ehrenbard, and S. Chapin (1987), Anomalous upper mantle beneath the Australian-Antarctic Discordance, *Earth Planet. Sci. Lett.*, *84*, 471–478.

Goff, J. A., Y. Ma, A. Shah, J. R. Cochran, and J.-C. Sempere (1997), Stochastic analysis of seafloor morphology on the

flanks of the Southeast Indian Ridge: The influence of ridge morphology on the formation of abyssal hills, *J. Geophys. Res.*, *102*, 15,521–15,534.
Gripp, A. E., and G. R. Gordon (1990), Current plate velocities relative to the hotspots incorporating the NUVEL-1 global plate motion model, *Geophys. Res. Lett.*, *17*(8), 1109–1112.
Harding, A. J., G. M. Kent, and J. A. Orcutt (1993), A multichannel seismic investigation of the upper crustal structure at 9°N on the East Pacific Rise: Implications for crustal accretion, *J. Geophys. Res.*, *98*, 13,925–13,944.
Heezen, B. C. (1960), The rift in the ocean floor, *Sci. Am.*, *203*, 99–110.
Hooft, E. E., and R. S. Detrick (1995), Relationship between axial morphology, crustal thickness, and mantle temperature along the Juan de Fuca and Gorda Ridges, *J. Geophys. Res.*, *100*, 22,499–22,508.
Hooft, E. E. E., H. Schouten, and R. S. Detrick (1996), Constraining crustal emplacement processes from the variation of seismic layer 2A thickness at the East Pacific Rise, *Earth Planet. Sci. Lett.*, *142*, 289–310.
Hooft, E. E., R. E. Detrick, and G. M. Kent (1997), Seismic structure and indicators of magma budget along the southern East Pacific Rise, *J. Geophys. Res.*, *102*, 27,319–27,340.
Hussenoeder, S. A., G. M. Kent, and R. S. Detrick (2002), Upper crustal seismic structure of the slow spreading Mid-Atlantic Ridge, 35°N: Constraints on volcanic emplacement processes, *J. Geophys. Res.*, *107*(B8), 2156, doi:10.1029/2001JB001691.
Kent, G. M., A. J. Harding, and J. A. Orcutt (1993a), Distribution of magma beneath the East Pacific Rise between the Clipperton transform and the 9°17′N deval from forward modeling of common depth point data, *J. Geophys. Res.*, *98*, 13,945–13,969.
Kent, G. M., A. J. Harding, and J. A. Orcutt (1993b), Distribution of magma beneath the East Pacific Rise near the 9°03′N overlapping spreading center from forward modeling of common depth point data, *J. Geophys. Res.*, *98*, 13,971–13,995.
Kent, G. M., A. J. Harding, J. A. Orcutt, R. S. Detrick, J. C. Mutter, and P. Buhl (1994), Uniform accretion of oceanic crust south of the Garrett transform at 14°15′S on the East Pacific Rise., *J. Geophys. Res.*, *99*, 9097–9116.
Klein, E. M., C. H. Langmuir, A. Zindler, H. Staudigel, and B. Hamelin (1988), Isotopic evidence of a mantle convecting boundary at the Australian-Antarctic discordance, *Nature*, *333*, 623–629.
Klein, E. M., C. H. Langmuir, and H. Staudigel (1991), Geochemistry of basalts from the Southeast Indian Ridge, 115°E-138°E, *J. Geophys. Res.*, *96*, 2089–2108.
Kuo, B. Y., and D. W. Forsyth (1988), Gravity anomalies of the ridge-transform system in the south Atlantic between 31 and 34.5°S: Upwelling centers and variations in crustal thickness, *Mar. Geophys. Res.*, *10*, 205–232.
Lin, J., G. M. Purdy, H. Schouten, J. C. Sempere, and C. Zervas (1990), Evidence from gravity data for focused magmatic accretion along the Mid-Atlantic Ridge, *Nature*, *344*, 627–632.
Ma, Y., and J. R. Cochran (1996), Transitions in axial morphology along the Southeast Indian Ridge, *J. Geophys. Res.*, *101*, 15,849–15,866.
Ma, Y., and J. R. Cochran (1997), Bathymetric roughness of the Southeast Indian Ridge: Implications for crustal accretion at intermediate spreading rate mid-ocean ridges, *J. Geophys. Res.*, *102*, 17,697–17,711.
MacDonald, K. C. (1986), The crest of the Mid-Atlantic Ridge: Models for crustal generation processes and tectonics, in *The Western North Atlantic Region*, edited by P. Vogt and B. Tucholke, pp. 51–68, Geol. Soc. of Am., Boulder, Colo.
MacDonald, K. C. (1989), Tectonic and magmatic processes on the East Pacific Rise, in *The Eastern Pacific Ocean and Hawaii*, edited by E. L. Winterer, D. M. Hussong, and R. W. Decker, pp. 93–110, Geol. Soc. of Am., Boulder, Colo.
Mahoney, J. J., D. W. Graham, D. M. Christie, K. T. M. Johnson, L. S. Hall, and D. L. Vonderhaar (2002), Between a hotspot and a cold spot: Isotopic variation in the Southeast Indian Ridge asthenosphere, 86°E-118°E, *J. Petrol.*, *43*, 1155–1176.
Malinverno, A. (1993), Transition between a valley and a high at the axis of the mid-ocean ridges, *Geology*, *21*, 639–642.
McDonald, M. A., S. C. Webb, J. A. Hildebrand, B. D. Cornuelle, and C. G. Fox (1994), Seismic structure and anisotropy of the Juan de Fuca ridge at 45°N, *J. Geophys. Res.*, *99*, 4857–4873.
Menard, H. W. (1960), The East Pacific Rise, *Science*, *132*, 1737–1746.
Morton, J. L., N. H. Sleep, W. R. Normark, and D. H. Tompkins (1987), Structure of the southern Juan de Fuca Ridge from seismic reflection records, *J. Geophys. Res.*, *92*, 11,315–11,326.
Mutter, J. C., S. M. Carbotte, W. Su, L. Xu, P. Buhl, R. S. Detrick, G. A. Kent, J. A. Orcutt, and A. J. Harding (1995), Seismic images of active magma systems beneath the East Pacific Rise between 17°05′ and 17°35′S, *Science*, *268*, 391–395.
Palmer, J., J. C. Sempere, D. M. Christie, and J. Phipps Morgan (1993), Morphology and tectonics of the Australian-Antarctic Discordance between 123°E and 128°E, *Mar. Geophys. Res.*, *15*, 121–152.
Phipps Morgan, J., and Y. J. Chen (1993), Dependence of ridge-axis morphology on magma supply and spreading rate, *Nature*, *364*, 706–708.
Purdy, G. M., L. S. L. Kong, G. L. Christeson, and S. C. Solomon (1992), Relationship between spreading rate and the seismic structure of mid-ocean ridges, *Nature*, *355*, 815–817.
Pyle, D. G. (1994), Geochemistry of mid-ocean ridge basalt within and surrounding the Australian-Antarctic Discordance, Ph.D. thesis, Oregon State Univ., Corvallis.
Rohr, K. M. M. (1994), Increase of seismic velocities in upper crust and hydrothermal circulation in the Juan de Fuca plate, *Geophys Res. Lett.*, *21*, 2163–2166.
Royer, J. Y., and D. T. Sandwell (1989), Evolution of the eastern Indian Ocean since the late Cretaceous: Constraints from Geosat altimetry, *J. Geophys. Res.*, *94*, 13,755–13,782.
Sempéré, J., J. R. Cochran, and SEIR Scientific Team (1997), The Southeast Indian Ridge between 88°E and 118°E: Variations in crustal accretion at constant spreading rate, *J. Geophys. Res.*, *102*(B7), 15,489–15,506.
Sinha, M. C., D. A. Navin, L. M. MacGregor, S. Constable, C. Pierce, A. White, G. Heinson, and M. A. Inglis (1997), Evidence for accumulated melt beneath the slow spreading Mid-Atlantic Ridge, in *Mid-Ocean Ridges: Dynamics of Processes Associated With Creation of New Ocean Crust*, edited by J. R. Cann, H. Elderfield, and A. Laughton, *Philos. Trans. R. Soc. London, Ser. A*, *355*, 233–253.
Sinton, J., R. Detrick, J. P. Canales, G. Ito, and M. Behn (2003), Morphology and segmentation of the western Galápagos Spreading Center, 90.5°–98°W: Plume-ridge interaction at an intermediate spreading ridge, *Geochem. Geophys. Geosyst.*, *4*(12), 8515, doi:10.1029/2003GC000609.
Small, C. (1994), A global analysis of mid-ocean ridge axial topography, *Geophys. J. Int.*, *116*, 64–84.

Small, C. (1995), Observations of ridge-hotspot interactions in the Southern Ocean, *J. Geophys. Res.*, *100*, 17,931–17,946.

Small, C. (1998), Global systematics of mid-ocean ridge axial morphology, in *Faulting and Magmatism at Mid-Ocean Ridges*, *Geophys. Monogr. Ser.*, vol. 106, edited by W. R. Buck et al., pp. 1–26, AGU, Washington, D. C.

Small, C., and L. V. Danyushevsky (2003), Plate-kinematic explanation for mid-oceanic-ridge depth discontinuities, *Geology*, *31*(5), 399–402.

Small, C., and D. T. Sandwell (1989), An abrupt change in ridge axis gravity with spreading rate, *J. Geophys. Res.*, *94*, 17,383–17,392.

Tolstoy, M., A. J. Harding, J. A. Orcutt, and J. Phipps Morgan (1995), Crustal thickness at the Australian Antarctic Discordance and neighboring Southeast Indian Ridge, *Eos Trans. AGU*, *76*(46), Fall Meet. Suppl., F570.

Vera, E. E., and J. B. Diebold (1994), Seismic imaging of layer 2A between 9°30′N and 10°N on the East Pacific Rise from two-ship wide-aperture profiles, *J. Geophys. Res.*, *99*, 3031–3041.

Vera, E. E., J. C. Mutter, P. Buhl, J. A. Orcutt, A. J. Harding, M. E. Kappus, R. S. Detrick, and T. M. Brocher (1990), The structure of 0- to 0.2-m.y.-old oceanic crust at 9°N on the East Pacific Rise from expanded spread profiles, *J. Geophys. Res.*, *95*, 15,529–15,556.

Wang, X., and J. R. Cochran (1993), Gravity anomalies, isostasy and mantle flow at the East Pacific Rise crest, *J. Geophys. Res.*, *98*, 19,505–19,531.

Weissel, J. K., and D. E. Hayes (1974), The Australian Antarctic Discordance: New results and implications, *J. Geophys. Res.*, *79*, 2579–2587.

Wessel, P., and W. H. F. Smith (1998), New improved version of Generic Mapping Tools released, *Eos Trans. AGU*, *79*, 579.

West, B. P., J.-C. Sempere, D. G. Pyle, J. Phipps Morgan, and D. M. Christie (1994), Evidence for variable upper mantle temperature and crustal thickness in and near the Australian-Antarctic Discordance, *Earth Planet. Sci. Lett.*, *128*, 135–153.

West, B. P., W. S. D. Wilcock, and J.-C. Sempere (1997), Three-dimensional structure of asthenospheric flow beneath the Southeast Indian Ridge, *J. Geophys. Res.*, *102*, 7783–7802.

Yale, M. M., and J. Phipps Morgan (1998), Asthenosphere flow model of hotspot-ridge interactions: A comparison of Iceland and Kerguelen, *Earth Planet. Sci. Lett*, *161*(1–4), 45–56.